

## PAPER

Cite this: *J. Mater. Chem. A*, 2017, 5, 18707High-rate capability of Na<sub>2</sub>FePO<sub>4</sub>F nanoparticles by enhancing surface carbon functionality for Na-ion batteries†Jesse S. Ko,<sup>a</sup> Vicky V. T. Doan-Nguyen,<sup>b,c</sup> Hyung-Seok Kim,<sup>a</sup> Xavier Petrisans,<sup>a</sup> Ryan H. DeBlock,<sup>a</sup> Christopher S. Choi,<sup>a</sup> Jeffrey W. Long<sup>d</sup> and Bruce S. Dunn<sup>e,\*</sup>

Metal phosphate compounds are considered promising candidates as positive electrode materials for Na-ion batteries because they offer higher cation-insertion potentials than analogous metal oxides. One such example is sodium iron fluorophosphate (Na<sub>2</sub>FePO<sub>4</sub>F), a compound that is typically synthesized by high-temperature solid-state routes. In this study, we prepare phase-pure Na<sub>2</sub>FePO<sub>4</sub>F using the polyol route, a low-temperature process that allows for the synthesis of nanoparticles (15–25 nm), a form that enhances Na-ion insertion kinetics and cycling stability. We then apply two methods to enhance the electronic conductivity of Na<sub>2</sub>FePO<sub>4</sub>F: (i) converting residual organic byproducts of the polyol synthesis to conductive carbon coatings; and (ii) preparing a nanocomposite with reduced graphene oxide. The resulting electrode materials are characterized in nonaqueous Na-ion electrolytes, assessing such metrics as specific capacity, rate capability, and cycling stability. A thorough electrochemical kinetics analysis is performed to deconvolve surface- vs. bulk Na-ion insertion as a function of composite structure. Specific capacities between 60–110 mA h g<sup>-1</sup> were achieved in galvanostatic charge–discharge tests when cycling in the range from 10C to C/10, respectively.

Received 30th June 2017  
Accepted 14th August 2017

DOI: 10.1039/c7ta05680j

rsc.li/materials-a

## 1. Introduction

Sodium-ion batteries (Na-ion, NIBs) are emerging as an alternative energy-storage technology to lithium-ion due to cost-effective advantages pertaining to the higher abundance and lower cost of sodium,<sup>1–7</sup> along with the opportunity to eliminate the need for copper current collectors (sodium does not alloy with aluminum).<sup>4,5,8–10</sup> A key remaining challenge is to develop a new generation of Na-ion cathode materials (positive electrode) that exhibit high capacity, very positive insertion potentials, and high-rate capability.<sup>1–3,11</sup> The most commonly studied materials for Na-ion cathodes comprise layered oxides such as O3 and P2 type compounds where O and P represent octahedral or trigonal prismatic coordination of Na-ions and 3 or 2 represent the number of distinguishable sodium layers.<sup>11,12</sup> Between these two

structures, P2 type compounds are known to exhibit higher specific capacities (~150–200 mA h g<sup>-1</sup>) and improved cycle life compared to O3 type compounds (~90–125 mA h g<sup>-1</sup>).<sup>11–14</sup> However, a new class of materials, in the form of phosphates and fluorophosphates, is emerging as high capacity, high potential (~120–150 mA h g<sup>-1</sup>, 2.5–4.5 V vs. Na/Na<sup>+</sup>) electrode materials and represents a promising direction for NIBs with enhanced rate performance over O3 and P2 type layered oxides (2–4 V vs. Na/Na<sup>+</sup>).<sup>4,6,7,14,15</sup>

The increased potential for metal (fluoro)phosphates vs. Na/Na<sup>+</sup> arises from the inductive effect of the phosphate or fluorophosphate polyanion.<sup>15,16</sup> The main obstacle for using these compounds is their highly insulating nature, where conductive coatings and nanostructured morphologies are essential for improving their electrochemical performance, specifically, their rate capability.<sup>17</sup> Whereas most electrode materials networked through the phosphate or fluorophosphate polyanion develop into tunneled structures (e.g., olivine NaFePO<sub>4</sub> and NASICON Na<sub>3</sub>Fe<sub>2</sub>(PO<sub>4</sub>)<sub>3</sub>), sodium iron fluorophosphate (Na<sub>2</sub>FePO<sub>4</sub>F) is one of the few layered fluorophosphate compounds.<sup>1–7,11,18</sup> Based on a one-electron process, 1 mol of Na<sup>+</sup> can be reversibly de-inserted from Na<sub>2</sub>FePO<sub>4</sub>F<sup>19</sup> by utilizing the Fe<sup>2+</sup>/Fe<sup>3+</sup> couple, leading to a high theoretical capacity of 124 mA h g<sup>-1</sup>. In addition, the unit cell of the oxidized compound is only 3.7% smaller than the fully reduced compound, making it attractive as a low-strain material with improvement for long-term cycling.<sup>19</sup>

<sup>a</sup>Department of Materials Science and Engineering, University of California, Los Angeles, CA 90095, USA. E-mail: bdunn@ucla.edu

<sup>b</sup>California NanoSystems Institute, University of California, Santa Barbara, CA 93106, USA

<sup>c</sup>Materials Research Laboratory, University of California, Santa Barbara, CA 93106, USA

<sup>d</sup>U.S. Naval Research Laboratory, Surface Chemistry Branch (Code 6170), Washington, DC, 20375, USA

<sup>e</sup>U.S. Naval Research Laboratory–National Research Council Postdoctoral Associate, Washington, DC, 20375, USA

† Electronic supplementary information (ESI) available. See DOI: 10.1039/c7ta05680j

The first report on reversible Li-ion insertion into  $\text{Na}_2\text{FePO}_4\text{F}$  nanoparticles ranging from 75–100 nm in size was identified by Ellis *et al.*,<sup>19</sup> where liquid-phase syntheses such as sol-gel and hydrothermal reactions were used to prepare this material.<sup>19,20</sup> The use of ionothermal synthesis in expressing  $\text{Na}_2\text{FePO}_4\text{F}$  at even smaller sizes ( $\sim 25$  nm) resulted in enhanced cycling stability for Na-ion systems; however, there has yet to be a report on how smaller particle sizes affect rate capability.<sup>21</sup> Although liquid-phase syntheses<sup>19–21</sup> and even a “green” synthesis of  $\text{Na}_2\text{FePO}_4\text{F}$ <sup>22</sup> are promising approaches, solid-state methods have been the most widely used, typically combined with post-synthesis carbon coating and high-energy ball milling to achieve optimized Na-ion insertion properties.<sup>23–29</sup> Fundamental studies on the mobility of Na-ions and its diffusion throughout the layered  $\text{Na}_2\text{FePO}_4\text{F}$  structure have also been reported and revealed the nature of this material’s electrochemical Na-ion insertion mechanism.<sup>30,31</sup>

In the research reported here, we combine the benefits of expressing  $\text{Na}_2\text{FePO}_4\text{F}$  at the nanoscale (15–20 nm) and carbonizing organic residuals from the polyol process to achieve high-rate capabilities coupled with high specific capacities in nonaqueous Na-ion electrolytes. The polyol route is a versatile synthetic route to prepare nanoparticles ranging from metals to metal oxides to even metal chalcogenides.<sup>32</sup> This method has several advantageous features<sup>32</sup> such as: (i) water-compatible solubility of metal-salt precursors; (ii) synthesis of phase-pure nanocrystalline materials at low temperatures ( $< 320$  °C; highest boiling point of polyols); and (iii) mild reducing conditions to prepare metals/oxides/phosphates in their reduced state, such as for the synthesis of  $\text{LiFePO}_4$ .<sup>32,33</sup> To further enhance charge-storage properties, several forms of carbon additives such as carbon nanotubes, carbon nanofibers, mesoporous carbon, and graphene have been used to prepare nanocomposites with ion-intercalation materials.<sup>34–36</sup> In the present paper, we report the fabrication of nanocomposites comprised of  $\text{Na}_2\text{FePO}_4\text{F}$  and reduced graphene oxide (rGO), as this conductive carbon additive<sup>36,37</sup> ensures high-rate capability. Electroanalytical methods are used to identify how both nanoscale  $\text{Na}_2\text{FePO}_4\text{F}$  and surface carbon improve rate capability for reversible Na-ion insertion.

## 2. Experimental

### 2.1. Synthesis of $\text{Na}_2\text{FePO}_4\text{F}$

Bulk ( $> 100$  nm)  $\text{Na}_2\text{FePO}_4\text{F}$  was synthesized using a solid-state reaction (NFPP-SSR) by grinding stoichiometric molar amounts of sodium bicarbonate ( $\text{NaHCO}_3$ , Sigma-Aldrich,  $\geq 99.5\%$ ), iron oxalate dihydrate ( $\text{FeC}_2\text{O}_4 \cdot 2\text{H}_2\text{O}$ , Sigma-Aldrich,  $\geq 99.99\%$ ), ammonium phosphate dibasic ( $(\text{NH}_4)_2\text{HPO}_4$ , Sigma-Aldrich,  $\geq 98\%$ ), and sodium fluoride ( $\text{NaF}$ , Alfa Aesar, 99.99%) with an agate mortar and pestle and subsequently heating at 200 °C for 2 h, then ramping up to 400 °C at a rate of 10 °C  $\text{min}^{-1}$  for an additional 4 h under forming gas ( $\text{N}_2/\text{H}_2$ ; 95 : 5, v/v). After this initial heat-treatment, the powders were re-ground to ensure intimate contact and then sealed in a quartz ampule under argon and heated at 500 °C for 6 h.

For the polyol synthesis of  $\text{Na}_2\text{FePO}_4\text{F}$  nanoparticles, a stoichiometric molar ratio (1 : 1 : 1 : 1; 2 mmol product) of iron acetate ( $\text{Fe}(\text{C}_2\text{H}_3\text{O}_2)_2$ , Sigma-Aldrich,  $\geq 99.99\%$ ), ammonium dihydrogen phosphate ( $\text{NH}_4\text{H}_2\text{PO}_4$ , Sigma-Aldrich, 99.999%), sodium acetate ( $\text{CH}_3\text{COONa}$ , Sigma-Aldrich,  $\geq 99.0\%$ ), and sodium fluoride ( $\text{NaF}$ , Alfa Aesar, 99.99%) were suspended in 50 mL of tetraethylene glycol (TTEG;  $\text{HO}(\text{CH}_2\text{CH}_2\text{O})_3\text{CH}_2\text{CH}_2\text{OH}$ , Sigma-Aldrich, 99%) in a 100 mL round bottom flask attached to a reflux condenser. The temperature of this solution was ramped at a rate of 2.5 °C  $\text{min}^{-1}$  up to 335 °C and held for 16 h while stirring constantly. The resultant solution underwent a series of wash and centrifugation steps using several aliquots of acetone to remove the TTEG and organic residuals to yield  $\text{Na}_2\text{FePO}_4\text{F}$  nanoparticles (NFPP-P). The NFPP-P nanoparticles were then dried under vacuum at 120 °C for 24 h to remove residual moisture. To carbonize the residual organics left on the surface, NFPP-P was heat-treated at 450 °C under an inert atmosphere (flowing argon) at a ramping rate of 10 °C  $\text{min}^{-1}$  and held for 5 min which led to volatilization of nearly all the organics while carbonizing the remaining 1–2 wt% to form a carbon-coating (NFPP-450/Ar).

Nanocomposites of NFPP-450/Ar with reduced graphene oxide (rGO) were prepared by mixing NFPP-450/Ar powder with graphene oxide (80/20 by weight). The graphene oxide solution was prepared using a modified hummers method (3.9 g  $\text{L}^{-1}$ ).<sup>38</sup> The mixture of NFPP-450/Ar and graphene oxide was sonicated for 1 h and then dried on a hot plate at 120 °C while stirring. This powdered mixture was then reduced under an inert atmosphere (argon) at 350 °C at a ramping rate of 5 °C  $\text{min}^{-1}$  and held for 2 h to obtain the nanocomposite, NFPP-rGO, by converting graphene oxide to rGO.<sup>37,39,40</sup>

### 2.2. Materials characterization

Transmission electron microscopy (TEM) images were taken with an FEI Technai T12 TEM (120 keV) using a carbon-coated copper grid as a substrate in which  $\text{Na}_2\text{FePO}_4\text{F}$  (suspended in ethanol,  $\sim 0.2$  g  $\text{L}^{-1}$ ) was drop-cast. X-ray analysis of the vacuum-dried powders were characterized with a Rigaku Miniflex II diffractometer using a  $\text{CuK}\alpha$  radiation source ( $\lambda = 1.5406$  Å) and corresponding crystallite sizes calculated by Scherrer’s analysis. X-ray diffraction was also performed using a synchrotron radiation source ( $\lambda = 0.2112$  Å) with a Perkin-Elmer amorphous Si-based 2D detector for rapid acquisition and was performed at the Advanced Photon Source 11-ID-B at Argonne National Laboratory.<sup>41</sup> NIST-traceable  $\text{CeO}_2$  standard powder was used to calibrate the experimental geometry of the measurements. The sample-to-detector distance for synchrotron XRD was calibrated to 952.276 mm. Thermogravimetric analysis/differential scanning calorimetry (TGA/DSC) was performed using an SDT Q600 from TA Instruments to measure the amount of organics and to characterize thermal properties of the synthesized materials. Samples were heated to 900 °C at a rate of 10 °C  $\text{min}^{-1}$  in flowing air (flow rate: 100 mL  $\text{min}^{-1}$ ). For argon heat-treatments, the samples were heated to 450 °C at a rate of 5 °C  $\text{min}^{-1}$  (flow rate of 200 mL  $\text{min}^{-1}$ ).

### 2.3. Electrochemical characterization

Electrochemical measurements were carried out in a two-electrode Swagelok® cell using a BioLogic VMP-3 Potentiostat with experiments conducted in an inert atmosphere (ultra-high purity argon) glovebox with oxygen and moisture levels <1 ppm. Sodium metal foil was used as the counter electrode and the electrolyte solution was 1 M sodium perchlorate (NaClO<sub>4</sub>, Alfa-Aesar, 99.8% anhydrous) in propylene carbonate : fluoroethylene carbonate (PC : FEC; 95 : 5, v/v) (FEC, Alfa-Aesar, 98%). The working electrodes were prepared by making a carbon slurry in *N*-methyl-2-pyrrolidone (NMP, Sigma-Aldrich, 99.5% anhydrous) consisting of 70% active material, 20% Super P carbon black and 10% polyvinylidene fluoride binder (PVDF, Kynar HSV 900). After grinding this mixture with an agate mortar and pestle, the slurry was doctor-bladed (10 μm-thick film) onto  $\frac{3}{8}$ " diameter stainless steel foils and the assembly was air-dried overnight, followed by vacuum drying at 120 °C overnight. The material loading on the electrode ranged from 1–2 mg cm<sup>-2</sup>. Cyclic voltammetry and galvanostatic cycling were performed using cutoff voltages of 4.0 and 2.0 V vs. Na/Na<sup>+</sup>. Cyclic voltammograms were obtained at sweep rates of 0.1–100 mV s<sup>-1</sup>; for galvanostatic cycling, the C-rates used ranged from C/10 to 20C, where current rates were normalized to the theoretical capacity of Na<sub>2</sub>FePO<sub>4</sub>F (124 mA h g<sup>-1</sup>). For NFPF-P, specific capacity was normalized to the combined active mass of Na<sub>2</sub>FePO<sub>4</sub>F and the 10% organic residuals. In the case for NFPF-450/Ar and NFPF-rGO, specific

capacities were normalized to the active mass of Na<sub>2</sub>FePO<sub>4</sub>F while also taking into account the 1–2 wt% conductive coating. Electrochemical impedance spectroscopy (EIS) was recorded before every experiment with an applied AC amplitude of 10 mV scanned over 100 mHz to 900 kHz.

## 3. Results and discussion

To the best of our knowledge, this is the first report to describe using the polyol synthesis route to prepare nanoparticulate sodium iron fluorophosphate, Na<sub>2</sub>FePO<sub>4</sub>F (NFPF-P). Fluorophosphates are typically made using solid-state reaction that require high synthesis temperatures (>700 °C) under inert/reducing atmospheres.<sup>23–28,30</sup> Unlike traditional solid-state routes, the polyol route is carried out at a markedly lower temperature (<320 °C) with an added benefit of the polyol medium serving as a mild reducing agent, which favors the preparation of metal fluorophosphates in their reduced state.<sup>32</sup> Transmission electron microscopy reveals particle sizes of NFPF-P ranging between 15–20 nm (Fig. 1a) whereas NFPF prepared by solid-state reaction (NFPF-SSR; Fig. S1†) is composed of larger agglomerates (up to 400 nm). After the polyol synthesis, NFPF-P is thoroughly washed with several aliquots of acetone, with the final product containing ~10 wt% of residual organics (verified by TGA; Fig. 1b). Differential scanning calorimetry of the NFPF-P nanoparticles shows

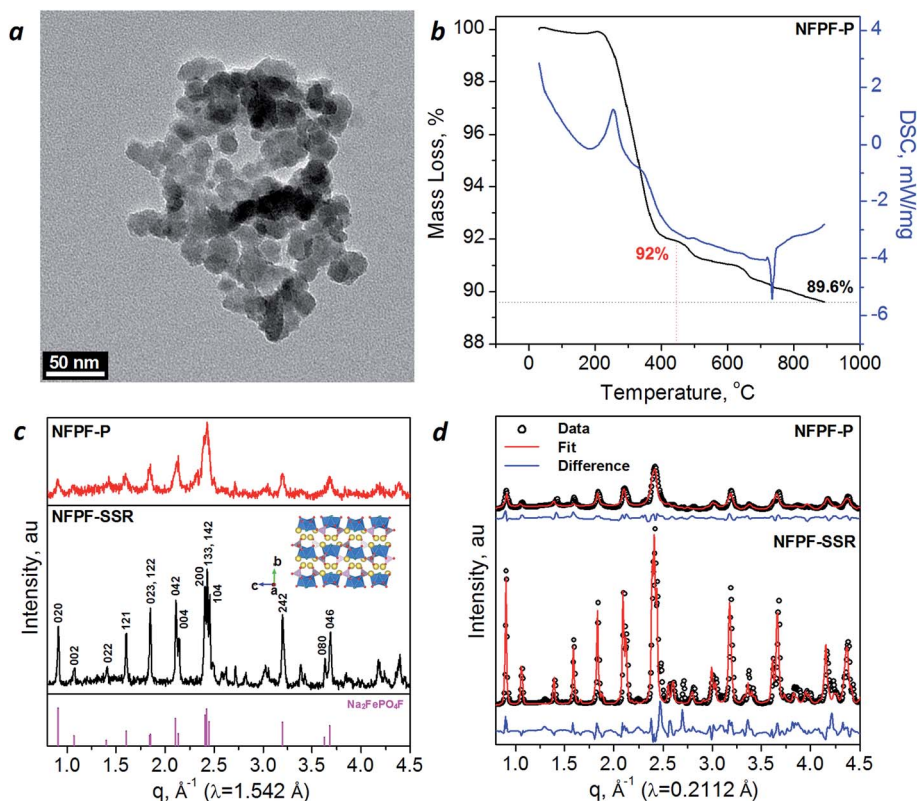


Fig. 1 (a) Transmission electron micrograph and (b) thermogravimetric analysis/differential scanning calorimetry of NFPF-P in air. The X-ray diffraction patterns of NFPF-P and NFPF-SSR using an X-ray source of (c) 1.5406 Å (inset shows a representation of the NFPF layered structure) and (d) 0.2112 Å.

a sharp endothermic peak positioned around 200 °C, which corresponds to volatilization of the organic residuals. Ramping to higher temperatures in air ( $\geq 700$  °C) oxidizes Fe(II) to Fe(III), as evidenced by the exothermic peak at  $\sim 700$  °C.

Phase purity and crystallinity of NFPF-P and NFPF-SSR were verified using XRD (Fig. 1c). Although most reported syntheses of NFPF use high temperatures ( $>800$  °C) to crystallize  $\text{Na}_2\text{FePO}_4\text{F}$  into its (orthorhombic) crystal habit, such conditions inevitably lead to large particles ( $\mu\text{m}$ -sized).<sup>23,24,26</sup> The lower temperature (335 °C) of the polyol process confers both phase pure crystallization and nanometric sizes ( $\sim 10$  nm) in accordance with broad XRD peaks (the crystal structure of  $\text{Na}_2\text{FePO}_4\text{F}$  is shown as an inset in Fig. 1c). Solid-state reaction of the precursors also yields phase purity, although accompanied by sharper diffraction peaks that arise from larger crystallite sizes ( $\sim 45$  nm). The calculated crystallite sizes of NFPF-P are in good agreement with the particle sizes measured from TEM analysis. In order to achieve a lower background-to-noise ratio, a synchrotron light source ( $\lambda = 0.2112$  Å) was utilized to obtain high-resolution diffraction spectra (Fig. 1d), along with Rietveld refinement to verify phase purity of both NFPF-P and NFPF-SSR. The performed Rietveld refinement also led to the classification of the following lattice parameters for both materials showing consistent crystal parameters (Table 1).

Expressing charge-storing materials in nanoscale forms alleviates solid-state ion-diffusion limitations of phosphate and fluorophosphates, which are known to be highly insulating materials.<sup>42</sup> However, another key step in improving charge-storage properties is to apply thin carbon coatings ( $\sim 1$ –3 wt%) to nanoscale materials that suffer from low electronic conductivity.<sup>17</sup> For example, the rate capability of  $\text{LiFePO}_4$  is drastically improved by carbothermally reducing organics at high temperatures to form conductive iron phosphocarbides/phosphides on the surface of the particles (1–3 wt%), that enhances surface electron transport.<sup>43</sup> For  $\text{Na}_2\text{FePO}_4\text{F}$ , a similar strategy was performed by adding sucrose or ascorbic acid during hydrothermal reaction to produce an organic coating on the surface, which was later carburized at high temperature (600–650 °C) under an inert atmosphere, leaving behind a conductive carbon coating ( $\sim 2$  wt%). In a similar fashion, a heat-treatment condition under Ar at 450 °C was used to remove a majority of the organics residuals from the polyol process ( $\sim 10\%$ , confirmed by TGA; Fig. S2†), while also carburizing the remaining organics ( $\sim 2$  wt%) into a mildly conductive carbon coating for NFPF-P; this material will now be denoted as NFPF-450/Ar. Although the XRD pattern of NFPF-450/Ar (Fig. S3a†) does not show any evidence of a second phase (e.g.  $\text{Fe}_2\text{O}_3$ ,  $\text{NaFePO}_4$ ), higher temperatures or longer dwell times induce carbothermal decomposition of  $\text{Na}_2\text{FePO}_4\text{F}$ ,

which leads to impurity phases such as  $\text{Fe}_2\text{O}_3$  and elemental Fe, even under an inert atmosphere (Fig. S3b†). To circumvent the elevated temperatures ( $>600$  °C under inert atmosphere) commonly used for high quality carbon coatings,<sup>44</sup> a nanocomposite comprising NFPF-450/Ar and reduced graphene oxide (rGO) is prepared in order to further enhance local electronic conductivity of the electrode without excessive heat-treatment temperatures.

In keeping with our previous work on incorporating metal oxides onto rGO,<sup>40,45</sup> we posit that during graphene oxide to rGO conversion (350 °C under Ar),<sup>37,39</sup> the carbon-coated NFPF-450/Ar particles adhere more strongly to the rGO, thus improving particle-to-particle wiring.<sup>36,45</sup> The X-ray analysis of NFPF-rGO reveals that phase purity is maintained (albeit higher background noise from 15–25° due to additional carbon content; Fig. S3a†), but average  $\text{Na}_2\text{FePO}_4\text{F}$  particle size increases to  $\sim 25$  nm (Fig. 2) as a consequence of the additional heat-treatment step.

The electrochemical properties of the series of NFPF samples were studied using cyclic voltammetry, a technique that provides information on rate capability and electrochemical reversibility. The voltammetric signature of all NFPF samples (NFPF-P, NFPF-450/Ar, and NFPF-rGO) consists of two coupled redox peaks (Fig. 3a), one at 2.9 V vs.  $\text{Na}/\text{Na}^+$  (denoted as A1–C1) and another at 3.1 V vs.  $\text{Na}/\text{Na}^+$  (denoted as A2–C2). The first redox peak at 2.9 V leads to the formation of  $\text{Na}_{1.5}\text{FePO}_4\text{F}$  whereas the second redox peak at 3.1 V corresponds to full oxidation of the  $\text{Fe}^{2+}/\text{Fe}^{3+}$  redox couple to  $\text{NaFePO}_4\text{F}$ .<sup>29</sup> The two different redox couples are dictated by the different  $\text{Na}^+$ -migration activation energies along the  $a$  [100] and  $c$  [001] axis (see inset in Fig. 1c).<sup>31</sup> On the basis of these voltammetric measurements, the rate capability can be assessed by integrating the voltammograms to measure specific capacity as a function of increasing sweep rates. As shown in Fig. 3b, NFPF-P achieves a high capacity of  $\sim 90$  mA h  $\text{g}^{-1}$  at 0.1 mV  $\text{s}^{-1}$  (charging time of 5.5 h) whereas at the same rate, NFPF-450/Ar and NFPF-rGO yields  $\sim 110$  mA h  $\text{g}^{-1}$ , which is 89% of theoretical capacity. For both NFPF-P and NFPF-450/Ar, there is a dramatic drop-off in specific capacity at rates higher than

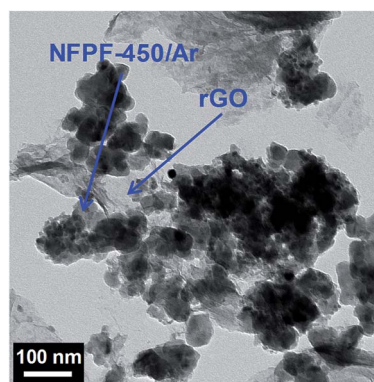


Fig. 2 Transmission electron micrograph of the nanocomposite comprising NFPF-450/Ar nanoparticles and reduced graphene oxide.

Table 1 Rietveld refined lattice parameters of NFPF-P and NFPF-SSR

Material	$a$ , Å	$b$ , Å	$c$ , Å
NFPF-P	5.10(2)	13.35(5)	11.61(9)
NFPF-SSR	5.10(7)	13.51(1)	11.48(6)

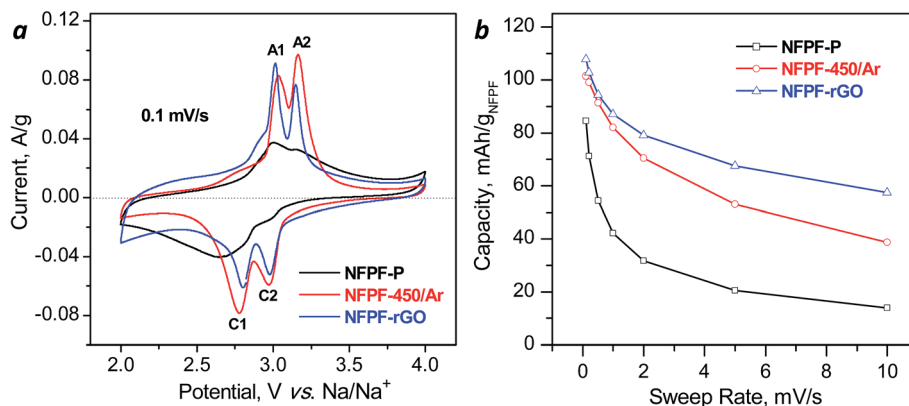


Fig. 3 (a) Cyclic voltammograms cycled between 2.0–4.0 V vs. Na/Na<sup>+</sup> at 0.1 mV s<sup>-1</sup> and (b) corresponding rate capability of NFPF-P, NFPF-450/Ar, and NFPF-rGO.

Table 2 Summary of peak separation ( $\Delta V = (V_{p,anodic} - V_{p,cathodic})$ ) at 0.1 mV s<sup>-1</sup> of NFPF-P, NFPF-450/Ar, and NFPF-rGO for both pairs of anodic and cathodic peaks (A1–C1 and A2–C2)

Material	$\Delta V (V_{p,A1} - V_{p,C1})$	$\Delta V (V_{p,A2} - V_{p,C2})$
NFPF-P	0.35	0.20
NFPF-450/Ar	0.26	0.19
NFPF-rGO	0.21	0.17

2 mV s<sup>-1</sup> whereas NFPF-rGO retains much of its capacity (~64%; 70 mA h g<sup>-1</sup>) at 10 mV s<sup>-1</sup> (charging time of 3.3 min).

The peak separation of a coupled redox reaction ( $\Delta V = V_{p,anodic} - V_{p,cathodic}$ ) relates to electrochemical kinetics reversibility that, in turn, broadly correlates to rate capability for charge storage—large peak separation leads to low-rate capability for insertion whereas small peak separation leads to high-rate capability.<sup>46</sup> The  $\Delta V$  for both coupled redox peaks consistently decreases (Table 2) with the incorporation of a carbon coating (NFPF-450/Ar) and subsequent rGO incorporation (NFPF-rGO). Within the electrochemically reversible regime (0.1 mV s<sup>-1</sup>), NFPF-rGO yields the smallest  $\Delta V$  of  $V_{p,A1} - V_{p,C1} = 0.21$

and  $V_{p,A2} - V_{p,C2} = 0.17$  for their accompanying redox peaks. Of note is the fact that systems reliant on solid-state ion diffusion show higher peak separations (Fig. S4†) at progressively higher sweep rates.

An analytical approach using cyclic voltammetry was applied to provide deeper insight into the charge storage mechanism for the series of materials investigated in this report (NFPF-P, NFPF-450/Ar, and NFPF-rGO). By cycling these materials from 0.1–5 mV s<sup>-1</sup>, a kinetic analysis (*b*-value analysis—dependence of current on the sweep rate) allows one to determine the dominating charge storage mechanism (surface-limited or diffusion-controlled). The following equation assumes that the current (*i*) obeys a power-law relationship with the sweep rate ( $\nu$ ):<sup>47</sup>

$$i = a\nu^b \quad (1)$$

where *a* and *b* are constants. The dominating charge-storage mechanism can be identified by extracting the *b*-value for a given redox potential from plots of log(*i*) vs. log( $\nu$ ). A *b*-value of 0.5 indicates charge storage that is controlled by solid-state diffusion of ions whereas a value of 1 is indicative of a surface-limited process. Although nanoparticles often circumvent solid-state diffusion limitations, the dominating

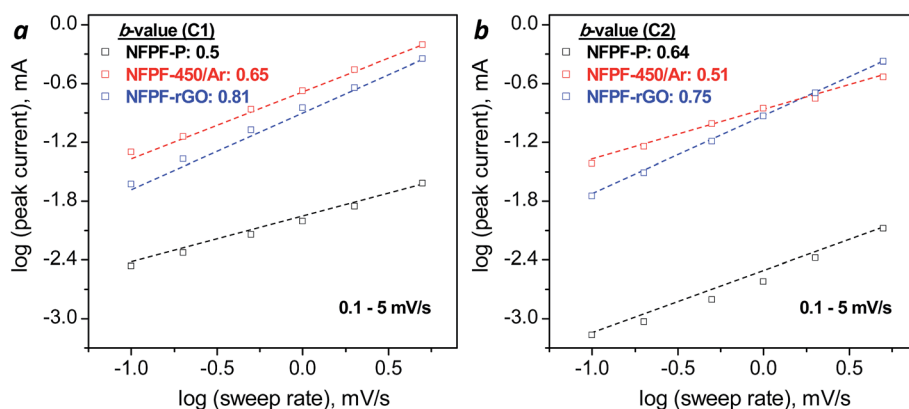


Fig. 4 Plot of log peak current vs. log sweep rate cycled between 0.1–5 mV s<sup>-1</sup> to yield *b*-values of NFPF-rGO corresponding to the (a) C1 and (b) C2 redox peaks.

charge-storage mechanism of NFPF-P and NFPF-450/Ar is diffusion-controlled in this range of sweep rates, where  $b$ -values were found to be  $\sim 0.55$  for both cathodic C1 and C2 peaks (Fig. 4a and b, respectively). The incorporation of conductive rGO directly leads to an improvement in diffusion limitations:  $b$ -value increases to 0.81 and 0.75 for C1 and C2 redox peaks, respectively. This increase in  $b$ -value suggests that the charge storage mechanism becomes more surface-limited, or for conditions that involve finite diffusion.<sup>48</sup> The  $b$ -values for all C1–A1 and C2–A2 paired redox peaks for the entire series of NFPF materials are shown in Fig. S5.†

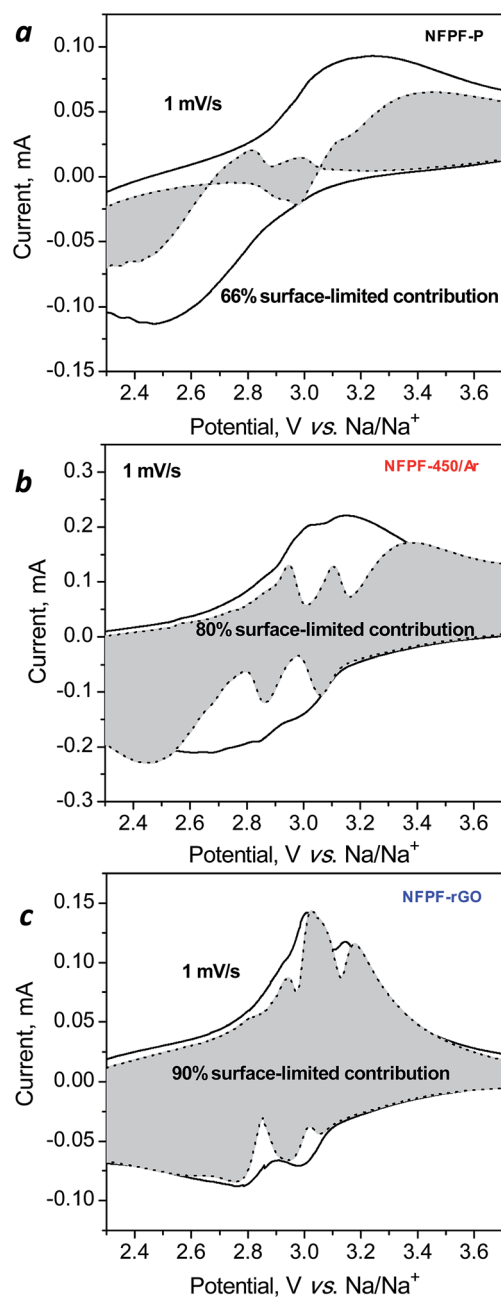


Fig. 5 Cyclic voltammograms of (a) NFPF-P, (b) NFPF-450/Ar, and (c) NFPF-rGO cycled at 1 mV s<sup>-1</sup> with representative shaded portions indicative of surface-limited current contribution.

The  $b$ -value analysis can be further extended to a more detailed version of the current power-law relationship:<sup>49</sup>

$$i(V) = k_1\nu^{1/2} + k_2\nu \quad (2)$$

where  $k_1$  and  $k_2$  are constants at a specific potential. The constants  $k_1$  and  $k_2$  are determined from a plot of  $i(V)\nu^{-1/2}$  vs.  $\nu^{1/2}$  and thus the surface-limited (shaded portion) and diffusion-limited contribution to the overall specific capacity can be determined. NFPF-P exhibits charge storage that shows a mixed surface- and diffusion-controlled mechanism (Fig. 5a) where the surface-limited contribution amounts to  $\sim 66\%$ ; for comparison, NFPF-SSR is predominately diffusion-controlled with only 20% surface-limited contribution (Fig. S6†). There is a monotonic increase in the surface-limited contribution where, after carbon-coating (NFPF-450/Ar), this contribution increases to 80% (Fig. 5b), and the nanocomposite (NFPF-rGO) exhibits a surface-limited contribution of 90% (Fig. 5c). The enhancement in charge-storage kinetics is mainly attributed to the improved local electronic conductivity within the composite electrode, achieved by incorporating rGO with NFPF-450/Ar.

Electrochemical impedance spectroscopy (EIS) was also applied to further our understanding of charge-storage characteristics. Measurements were recorded at open-circuit potential for cells containing NFPF-P, NFPF-450/Ar, or NFPF-rGO electrodes. Nyquist plots of the experimental data were fitted using an equivalent-circuit model composed of a series resistance ( $R_s$ ) at high frequencies, a charge-transfer resistance ( $R_{CT}$ ) in parallel with a constant-phase element (CPE), a Warburg impedance ( $Z_w$ ), and an infinite capacitance ( $C_{int}$ ); see Fig. 6.<sup>50–52</sup> The high-frequency semicircle corresponds to charge-transfer resistance for electrons and Na-ions across the electrode–electrolyte interface, carbon-particle interfaces and particle–particle contact; values for  $R_{CT}$  are summarized in Table 3.<sup>50–52</sup> The trend in  $R_{CT}$  values shows that carbon-coating alone does not significantly reduce charge-transfer resistance, whereas the additional step of combining carbon-coated NFPF

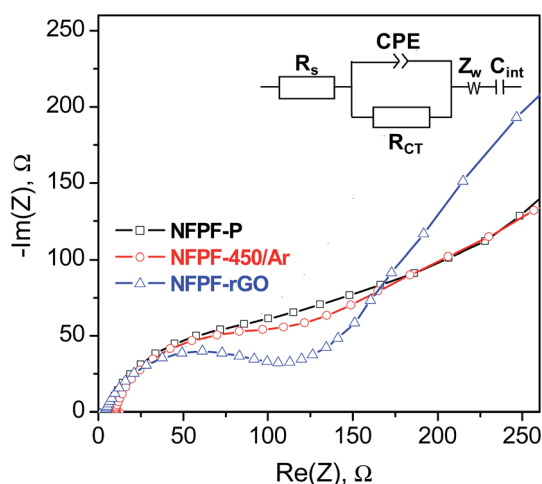


Fig. 6 Nyquist plot of NFPF-P, NFPF-450/Ar, and NFPF-rGO fitted by the equivalent circuit model shown in the inset.

**Table 3** Impedance parameters obtained from the equivalent-circuit model

Electrode material	$R_{CT}$ , $\Omega$	$\sigma$ , $\Omega \text{ s}^{-1/2}$	$D_{\text{Na}^+}$ , $\text{cm}^2 \text{ s}^{-1}$
NFPF-P	130	361	$3.70 \times 10^{-14}$
NFPF-450/Ar	113	280	$6.16 \times 10^{-14}$
NFPF-rGO	92	166	$1.74 \times 10^{-13}$

with rGO in a nanocomposite enhances charge-transfer properties.

The slope observed in the low-frequency range, which we assign to Warburg impedance,  $Z_w$ , was used to calculate the  $\text{Na}^+$  diffusion coefficient ( $D_{\text{Na}^+}$ ) in the composite,<sup>29,53,54</sup> following the general equation:<sup>55</sup>

$$D_{\text{Na}^+} = \frac{R^2 T^2}{2A^2 n^4 F^4 C^2 \sigma^2} \quad (3)$$

where  $R$  is the ideal gas constant ( $8.314 \text{ J mol}^{-1} \text{ K}^{-1}$ ),  $T$  is the ambient temperature (298.15 K),  $A$  is the cross-sectional surface area of the electrode ( $0.713 \text{ cm}^2$ ),  $n$  is the number of electrons per molecule during intercalation,  $F$  is the Faraday constant ( $96485 \text{ C mol}^{-1}$ ),  $C$  is the concentration of  $\text{Na}^+$  ( $3.80 \times 10^{-3} \text{ mol cm}^{-3}$ ),<sup>29</sup> and  $\sigma$  is the Warburg coefficient ( $\Omega \text{ s}^{-1/2}$ ). The Warburg coefficient is determined from the following relationship:

$$\text{Re}(Z) = R_s + R_{CT} + \sigma \omega^{-1/2} \quad (4)$$

where  $\omega$  is the angular frequency; therefore, the slope from a plot of  $\text{Re}(Z)$  vs.  $\omega^{-1/2}$  (Fig. S7†) provides  $\sigma$  values, which can be used to calculate  $D_{\text{Na}^+}$  for the series of NFPF electrodes (Table 3). We observe that with lower  $R_{CT}$ , the calculated  $D_{\text{Na}^+}$  increases; for example, NFPF-rGO exhibits much higher  $D_{\text{Na}^+}$  accompanied by a smaller charge-transfer resistance. Combining NFPF and rGO results in a 5× improvement in  $D_{\text{Na}^+}$  values, which implies that ion transport is significantly enhanced within this composite electrode structure.

To assess the electrochemical performance of the NFPF-rGO samples, galvanostatic cycling was performed within cut-off voltages of 2.0 and 4.0 V vs.  $\text{Na}/\text{Na}^+$ ; galvanostatic discharge curves and corresponding capacity-rate trends for NFPF-P and NFPF-450/Ar are shown in Fig. S8 and S9,† respectively. The electrochemical performance of NFPF-rGO was determined at varying C-rates (C/10–20C) and the charge–discharge curves are shown in Fig. 7a. This material exhibits two voltage plateaus situated at 2.8 and 3.0 V vs.  $\text{Na}/\text{Na}^+$  (phase transition from  $\text{Na}_2\text{FePO}_4\text{F}$  to  $\text{Na}_{1.5}\text{FePO}_4\text{F}$  to  $\text{NaFePO}_4\text{F}$ ), consistent with the coupled redox peaks observed in the CVs earlier. A high capacity of  $110 \text{ mA h g}^{-1}$  is achieved at C/10; at rates of 1C and 10C, NFPF-rGO provides a capacity of 90 and  $60 \text{ mA h g}^{-1}$ , respectively (Fig. 7b). Along with the high capacities, coulombic efficiencies greater than 95% are achieved throughout the entire range of C-rates. Moreover, long-term cycling at 10C shows 70% capacity retention after 5000 cycles (Fig. 7c).

Prior investigations of  $\text{Na}_2\text{FePO}_4\text{F}$  synthesized as several hundred nanometers to micron-sized particles showed high specific capacity at low C-rates ( $\sim\text{C}/10$ ,  $\sim 110\text{--}120 \text{ mA h g}^{-1}$ ),

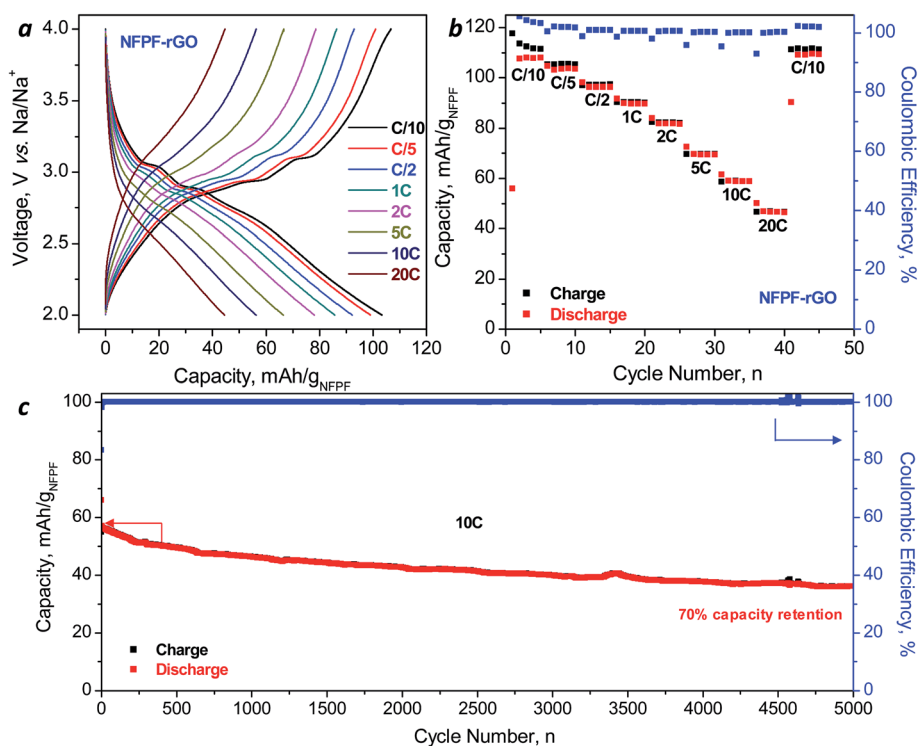


**Fig. 7** (a) Galvanostatic charge–discharge curves with imposed C-rates ranging between C/10–20C and (b) corresponding specific capacities and coulombic efficiencies of NFPF-rGO. (c) Long-term cycling of NFPF-rGO at 10C for 5000 cycles.

with moderate rate capability ( $\sim 10\text{C}$ ,  $\sim 20\text{--}25\text{ mA h g}^{-1}$ ) achieved by utilizing additional processing protocols such as high-energy ball milling,<sup>29</sup> carbon-coating,<sup>23,24</sup> and preparing carbon-coated hollow particles.<sup>25</sup> As described herein, combining nanoscale carbon-coated  $\text{Na}_2\text{FePO}_4\text{F}$  with rGO yields a material that exhibits high-rate capability for Na-ion insertion (specific capacities of  $\sim 60\text{ mA h g}^{-1}$  achieved at  $10\text{C}$ ). These results further demonstrate the advantages of incorporating nanoscale charge-storing materials with rGO, analogous to trends we previously reported for pseudocapacitive charge-storage with  $\text{MoO}_2\text{-rGO}$  nanocomposites cycled in a Li-ion electrolyte and  $\text{NaTi}_2(\text{PO}_4)_3$  in a Na-ion electrolyte.<sup>40,45</sup>

## 4. Conclusions

In this present work, we show that intimately integrating nanometric  $\text{Na}_2\text{FePO}_4\text{F}$  with conductive carbon components (carbon coatings produced by pyrolysis of organic byproducts and/or rGO) yields previously unrealized rate capability for Na-ion charge storage with this active material. Kinetics analysis of the cyclic voltammetric data shows that although diffusion-limitations are inherent for nanosized NFPF-P, charge-storage becomes more surface-limited with the combination of carbon coating and integration of rGO. Impedance spectroscopy confirms that  $R_{\text{CT}}$  is lower for nanocomposite NFPF-rGO and  $D_{\text{Na}^+}$  increases  $\sim 5\times$  compared to NFPF-P. In galvanostatic tests, the NFPF-rGO composite achieved a capacity of  $110\text{ mA h g}^{-1}$  at  $\text{C}/10$  and exhibited high-rate capability, where  $60\text{ mA h g}^{-1}$  was retained even at a challenging rate of  $10\text{C}$  with stable cycling.

## Conflicts of interest

There are no conflicts to declare.

## Acknowledgements

The authors acknowledge the financial support from the Navy Undersea Research Program (N00014-13-1-0605) and also by the U.S. Office of Naval Research (N00014-16-1-2164). This research used resources of the Advanced Photon Source, a U.S. Department of Energy (DOE) Office of Science User Facility operated by Argonne National Laboratory under Contract No. DE-AC02-06CH11357. The X-ray scattering experiments were performed at APS 11-ID-B under GUP-45245. J.S.K. is presently a NRL-NRC Postdoctoral Associate. V.D.N. is supported by the University of California President's Postdoctoral Fellowship and the University of California, Santa Barbara California NanoSystems Institute Elings Prize Fellowship. The authors are grateful to Dr Debra Rolison (U.S. Naval Research Laboratory, Washington, D.C. USA) for insightful discussions during the preparation of this manuscript.

## References

- 1 N. Yabuuchi, K. Kubota, M. Dahbi and S. Komaba, *Chem. Rev.*, 2014, **114**, 11636–11682.
- 2 M. D. Slater, D. Kim, E. Lee and C. S. Johnson, *Adv. Funct. Mater.*, 2013, **23**, 947–958.
- 3 S. W. Kim, D. H. Seo, X. Ma, G. Ceder and K. Kang, *Adv. Energy Mater.*, 2012, **2**, 710–721.
- 4 V. Palomares, P. Serras, I. Villaluenga, K. B. Hueso, J. Carretero-González and T. Rojo, *Energy Environ. Sci.*, 2012, **5**, 5884–5901.
- 5 V. Palomares, M. Casas-Cabanas, E. Castillo-Martínez, M. H. Han and T. Rojo, *Energy Environ. Sci.*, 2013, **6**, 2312–2337.
- 6 H. Kim, H. Kim, Z. Ding, M. H. Lee, K. Lim, G. Yoon and K. Kang, *Adv. Energy Mater.*, 2016, **6**, 1600943.
- 7 J.-Y. Hwang, S.-T. Myung and Y.-K. Sun, *Chem. Soc. Rev.*, 2017, **46**, 3529–3614.
- 8 K. Kubota and S. Komaba, *J. Electrochem. Soc.*, 2013, **162**, A2538–A2550.
- 9 H. Kang, Y. Liu, K. Cao, Y. Zhao, L. Jiao, Y. Wang and H. Yuan, *J. Mater. Chem. A*, 2015, **3**, 17899–17913.
- 10 W. Luo, F. Shen, C. Bommier, H. Zhu, X. Ji and L. Hu, *Acc. Chem. Res.*, 2016, **49**, 231–240.
- 11 M. H. Han, E. Gonzalo, G. Singh and T. Rojo, *Energy Environ. Sci.*, 2015, **8**, 81–102.
- 12 C. Delmas, C. Fouassier and P. Hagenmuller, *Physica B+C*, 1980, **99**, 81–85.
- 13 Y. Wang, X. Yu, S. Xu, J. Bai, R. Xiao, Y. S. Hu, H. Li, X. Q. Yang, L. Chen and X. A. Huang, *Nat. Commun.*, 2013, **4**, 2365.
- 14 N. Yabuuchi, M. Kajiyama, J. Iwatate, H. Nishikawa, S. Hitomi, R. Okuyama, R. Usui, Y. Yamada and S. Komaba, *Nat. Mater.*, 2012, **11**, 512–517.
- 15 C. Masquelier and L. Croguennec, *Chem. Rev.*, 2013, **113**, 6552–6591.
- 16 A. Gutierrez, N. A. Benedek and A. Manthiram, *Chem. Mater.*, 2013, **25**, 4010–4016.
- 17 J. Wang and S. Xueliang, *Energy Environ. Sci.*, 2012, **5**, 5163.
- 18 R. Rajagopalan, B. Chen, Z. Zhang, X.-L. Wu, Y. Du, Y. Huang, B. Li, Y. Zong, J. Wang, G.-H. Nam, M. Sindoro, S. X. Dou, H. K. Liu and H. Zhang, *Adv. Mater.*, 2017, **29**, 1605694.
- 19 B. L. Ellis, W. R. M. Makahnouk, Y. Makimura, K. Toghill and L. F. Nazar, *Nat. Mater.*, 2007, **6**, 749–753.
- 20 B. L. Ellis, W. R. M. Makahnouk, W. N. Rowan-Weetaluktuk, D. H. Ryan and L. F. Nazar, *Chem. Mater.*, 2010, **22**, 1059–1070.
- 21 N. Recham, J.-N. Chotard, L. Dupont, K. Djellab, M. Armand and J.-M. Tarascon, *J. Electrochem. Soc.*, 2009, **156**, A993.
- 22 X. Deng, W. Shi, J. Sunarso, M. Liu and Z. Shao, *ACS Appl. Mater. Interfaces*, 2017, **9**, 16280–16287.
- 23 Y. Kawabe, N. Yabuuchi, M. Kajiyama, N. Fukuhara, T. Inamasu, R. Okuyama, I. Nakai and S. Komaba, *Electrochemistry*, 2012, **80**, 80–84.
- 24 Y. Kawabe, N. Yabuuchi, M. Kajiyama, N. Fukuhara, T. Inamasu, R. Okuyama, I. Nakai and S. Komaba, *Electrochem. Commun.*, 2011, **13**, 1225–1228.
- 25 A. Langrock, Y. Xu, Y. Liu, S. Ehrman, A. Manivannan and C. Wang, *J. Power Sources*, 2013, **223**, 62–67.

- 26 J. Zhou, J. Zhou, Y. Tang, Y. Bi, C. Wang, D. Wang and S. Shi, *Ceram. Int.*, 2013, **39**, 5379–5385.
- 27 N. V. Kosova, V. R. Podugolnikov, E. T. Devyatkina and A. B. Slobodyuk, *Mater. Res. Bull.*, 2014, **60**, 849–857.
- 28 J. Yan, X. Liu and B. Li, *Electrochem. Commun.*, 2015, **56**, 46–50.
- 29 M. Law, V. Ramar and P. Balaya, *RSC Adv.*, 2015, **5**, 50155–50164.
- 30 W. Song, J. Xiaobo, W. Zhengping, Y. Zhu, Y. Yao, K. Huangfu, Q. Chen and C. E. Banks, *J. Mater. Chem. A*, 2014, **2**, 2571.
- 31 R. Tripathi, S. M. Wood, M. S. Islam and L. F. Nazar, *Energy Environ. Sci.*, 2013, **6**, 2257–2264.
- 32 H. Dong, Y.-C. Chen and C. Feldmann, *Green Chem.*, 2015, **17**, 4107–4132.
- 33 D.-H. Kim and J. Kim, *Electrochem. Solid-State Lett.*, 2006, **9**, A439.
- 34 D. S. Su and R. Schlögl, *ChemSusChem*, 2010, **3**, 136–168.
- 35 J. Ni and Y. Li, *Adv. Energy Mater.*, 2016, **6**, 1600278.
- 36 R. Raccichini, A. Varzi, S. Passerini and B. Scrosati, *Nat. Mater.*, 2015, **14**, 271–279.
- 37 Y. Zhou, Q. Bao, L. A. L. Tang, Y. Zhong and K. P. Loh, *Chem. Mater.*, 2009, **21**, 2950–2956.
- 38 W. S. Hummers and R. E. Offerman, *J. Am. Chem. Soc.*, 1958, **80**, 1339.
- 39 A. Ganguly, S. Sharma, P. Papakonstantinou and J. Hamilton, *J. Phys. Chem. C*, 2011, **115**, 17009–17019.
- 40 J. S. Ko, C. S. Choi, B. Dunn and J. W. Long, *J. Electrochem. Soc.*, 2017, **164**, A2124–A2130.
- 41 X. Qiu, J. W. Thompson and S. J. L. Billinge, *J. Appl. Crystallogr.*, 2004, **37**, 678.
- 42 A. Manthiram, A. Vadivel Murugan, A. Sarkar and T. Muraliganth, *Energy Environ. Sci.*, 2008, **1**, 621.
- 43 Y.-H. Rho, L. F. Nazar, L. Perry and D. Ryan, *J. Electrochem. Soc.*, 2007, **154**, A283.
- 44 A. Ponrouch, A. R. Goñi, M. T. Sougrati, M. Ati, J.-M. Tarascon, J. Nava-Avendaño and M. R. Palacin, *Energy Environ. Sci.*, 2013, **6**, 3363–3371.
- 45 H.-S. Kim, J. B. Cook, S. H. Tolbert and B. Dunn, *J. Electrochem. Soc.*, 2015, **162**, A5083–A5090.
- 46 V. Augustyn, J. Come, M. A. Lowe, J. W. Kim, P.-L. Taberna, S. H. Tolbert, H. D. Abruña and B. Dunn, *Nat. Mater.*, 2013, **12**, 1882–1888.
- 47 H. Lindström, S. Södergren, A. Solbrand, H. Rensmo, J. Hjelm, A. Hagfeldt and S.-E. Lindquist, *J. Phys. Chem. B*, 1997, **101**, 7717–7722.
- 48 A. T. Hubbard, *J. Electroanal. Chem. Interfacial Electrochem.*, 1969, **22**, 165–174.
- 49 T.-C. Liu, W. G. Pell and B. E. Conway, *J. Electrochem. Soc.*, 1998, **145**, 1882–1888.
- 50 M. D. Levi, G. Salitra, B. H. Markovsky Teller, D. Aurbach, U. Heider and L. Heider, *J. Electrochem. Soc.*, 1999, **146**, 1279–1289.
- 51 M. D. Levi and D. Aurbach, *J. Phys. Chem. B*, 1997, **101**, 4630–4640.
- 52 D. Lu, W. Li, X. Zuo, Z. Yuan and Q. Huang, *J. Phys. Chem. C*, 2007, **111**, 12067–12074.
- 53 F. Gao and Z. Tang, *Electrochim. Acta*, 2008, **53**, 5071–5075.
- 54 B. Jin, E. M. Jin, K.-H. Park and H.-B. Gu, *Electrochem. Commun.*, 2008, **10**, 1537–1540.
- 55 A. J. Bard and L. R. Faulkner, *Electrochemical Methods: Fundamentals and Applications*, John Wiley & Sons, New York, NY, 2nd edn, 2001.